Inorganic Chemistry
Article
pubs.acs.org/IC

Experimental and Computational X-ray Emission Spectroscopy as a Direct Probe of Protonation States in Oxo-Bridged Mn^{IV} Dimers Relevant to Redox-Active Metalloproteins

Benedikt Lassalle-Kaiser,[†] Thaddeus T. Boron III,[‡] Vera Krewald,[§] Jan Kern,[†,∥] Martha A. Beckwith,[§,⊥] Mario U. Delgado-Jaime,[§] Henning Schroeder,[†] Roberto Alonso-Mori,[∥] Dennis Nordlund,[∥] Tsu-Chien Weng,[∥] Dimosthenis Sokaras,[∥] Frank Neese,[§] Uwe Bergmann,[∥] Vittal K. Yachandra,[†] Serena DeBeer,*[,§,⊥] Vincent L. Pecoraro,*[,‡] and Junko Yano*[,†]

[†]Physical Biosciences Division, Lawrence Berkeley National Laboratory, Berkeley, California 94720, United States
[‡]Department of Chemistry, University of Michigan, Ann Arbor, Michigan 48109, United States
[§]Max Planck Institute for Chemical Energy Conversion, Stiftstrasse 34-36, 45470 Mülheim an der Ruhr, Germany
[∥]SLAC National Accelerator Laboratory, Menlo Park, California 94025, United States
[⊥]Department of Chemistry and Chemical Biology, Cornell University, Ithaca, New York 14853, United States

Supporting Information

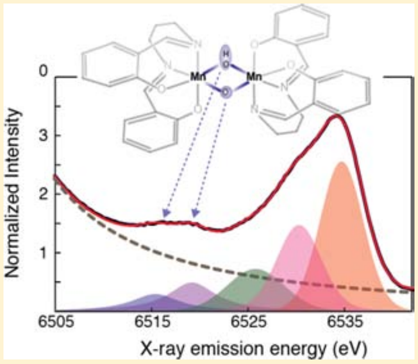

ABSTRACT: The protonation state of oxo bridges in nature is of profound importance for a variety of enzymes, including the Mn_4CaO_5 cluster of photosystem II and the Mn_2O_2 cluster in Mn catalase. A set of dinuclear bis-μ-oxo-bridged Mn^{IV} complexes in different protonation states was studied by Kβ emission spectroscopy to form the foundation for unraveling the protonation states in the native complex. The valence-to-core regions (valence-to-core XES) of the spectra show significant changes in intensity and peak position upon protonation. DFT calculations were performed to simulate the valence-to-core XES spectra and to assign the spectral features to specific transitions. The K$\beta_{2,5}$ peaks arise primarily from the ligand 2p to Mn 1s transitions, with a characteristic low energy shoulder appearing upon oxo-bridge protonation. The satellite Kβ'' peak provides a more direct signature of the protonation state change, since the transitions originating from the 2s orbitals of protonated and unprotonated μ-oxo bridges dominate this spectral region. The energies of the Kβ'' features differ by ~3 eV and thus are well resolved in the experimental spectra. Additionally, our work explores the chemical resolution limits of the method, namely, whether a mixed (μ-O)(μ-OH_2) motif can be distinguished from a symmetric (μ-OH)$_2$ one. The results reported here highlight the sensitivity of Kβ valence-to-core XES to single protonation state changes of bridging ligands, and form the basis for further studies of oxo-bridged polymetallic complexes and metalloenzyme active sites. In a complementary paper, the results from X-ray absorption spectroscopy of the same Mn^{IV} dimer series are discussed.

INTRODUCTION

Protonation states of oxo-bridging and terminal ligands (O^{2-}, OH^-, OH_2) often control catalytic function in inorganic and bioinorganic catalysts, by modulating the charge density distribution between the metals and ligands, the pK_a of bound water/hydroxide, and the covalency between metals and ligands. Examples of such systems include catalysts involved in O_2 association and dissociation reactions. In the hydrogen peroxide disproportionation reaction, catalyzed by Mn catalase, oxo bridges undergo protonation and deprotonation events that are essential to their physiological function, and certain protonation states are known to inhibit the catalytic reaction.[1,2] In the water-oxidation reaction catalyzed by the Mn_4CaO_5 cluster in photosystem II, protonation state changes in the bridging oxygen (μ-oxo or μ-hydroxo) and/or a terminal substrate water as aqua or hydroxo have been proposed during the four electron redox chemistry.[3−5]

More generally, protonation/deprotonation reactions of metal centers in biology are now recognized as important processes that moderate reaction chemistry. For example, copper oxo/hydroxo/peroxo complexes play vital roles in respiration, such as in hemocyanin,[6] in biological metabolic pathways such as catechol oxidase activity[7] or activation of aliphatic C−H bonds by dopamine β-monooxygenase, peptidylglycine α-amidating enzyme, and particulate methane monooxygenase.[8] Another important reaction is the reduction of ribonucleotides to the deoxy form in ribonucleotide reductase catalyzed by the FeFe or FeMn cluster, in which the O_2 activation by the FeMn cluster may be accompanied by the protonation state changes at the bridging oxygen.[9] It is also known that FeFe clusters in soluble methane monooxygenase

Received: April 3, 2013
Published: October 25, 2013

dx.doi.org/10.1021/ic400821g | *Inorg. Chem.* 2013, 52, 12915−12922

catalyze the hydroxylation of methane to methanol.[10−14] Understanding these events requires techniques that are sensitive enough to differentiate species that differ only by a single proton.

Numerous small molecule mimics exist in the literature for these biological systems.[15] Model compounds assessing the properties and reactivities of $Mn^{IV}{-}OH$ and $Mn^{IV}{=}O$ as well as $Fe^{IV}{-}OH$ and $Fe^{IV}{=}O$ species have been reported by several groups.[16−21] Que and co-workers have examined Fe complexes that are remarkable for their H-atom abstraction capabilities.[22,23] In some systems, it is possible to resolve the protonation state of oxo-bridged species through single-crystal X-ray crystallography[6] where unusually long or short M−O and M−OH bonds have been reported.[14,24] However, the chemical assignment of these unusual bond distances and associated protonation states is not always straightforward and could be further strengthened using a technique that has more direct sensitivity to the protonation event.

Several techniques have the potential to detect a single protonation event, while few of them can directly and selectively probe the protons in the first coordination sphere of a transition metal ion. Potential methods include vibrational spectroscopy[25] and ligand sensitive EPR techniques such as ENDOR (electron nuclear double resonance), ESEEM (electron spin echo envelope modulation), and HYSCORE (hyperfine sublevel correlation).[26,27] The advantage of X-ray-based methods over EPR techniques is their element specificity and that they are not restricted by the spin states of the compounds.

In two complementary papers[28] we explore the sensitivity of both X-ray absorption (XAS) and X-ray emission spectroscopy (XES) to changes in ligand protonation state. XAS can serve as an indirect probe of the protonation state through changes in local symmetry and metal−ligand bond distances at the catalytic site.[29] The assignment of protonation states by XAS is further strengthened by close correlation to theory, as explored in the preceding paper.[28]

XES is complementary to XAS and provides a direct probe of the filled molecular orbitals. In a $K\beta$ XES spectrum, the "main line" features, $K\beta_{1,3}$ and $K\beta'$, correspond to a transition from a metal 3p orbital to a metal 1s hole (Figure 1). Due to a strong contribution from 3p−3d exchange contribution, this region of the spectrum is dominantly influenced by the number of unpaired spins of the metal and hence its oxidation and/or spin state. To higher energy is the valence-to-core region (or also called $K\beta_{2,5}$ and $K\beta''$ features, Figure 1). These features correspond primarily to transitions from ligand 2p and 2s orbitals, respectively, and as such contain direct information about the ligand identities.[30−36]

In this work, the use of XES as a sensitive probe of single protonation events at bridging oxygen atoms is explored. A set of homologous dinuclear Mn^{IV} complexes that were initially synthesized by Baldwin et al.,[29] in which the protonation state of the bridging oxygen atoms was changed systematically, is used as a test set (see Figure 2, Chart 1). This series serves as a model system to study the nature of protonation state changes in oxo bridges. A combination of XES data and DFT calculations provides a detailed understanding of the origin of valence-to-core emission peaks, making XES an important tool to resolve protonation states of bridging oxygen atoms in biological catalysts. The technique also allows us to differentiate between two possible structures for the doubly protonated species, namely, a bis-μ-hydroxo vs a μ-oxo-μ-aqua bridged

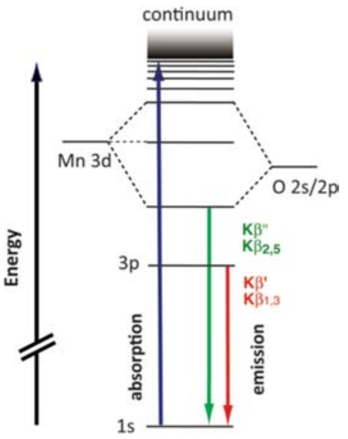

Figure 1. Energy diagram representing the X-ray absorption and emission preocesses at the K-edge of Mn. Blue arrow: absorption of a photon, exciting a 1s-electron into the continuum, leaving a 1s-hole. Green arrow: relaxation of ligand 2s/2p electron into the 1s-hole, emitting a photon in the $K\beta''$ or $K\beta_{2,5}$ energy range. Red arrow: relaxation of a metal 3p electron into the 1s-hole, emitting a photon in the $K\beta'$ or $K\beta_{1,3}$ energy range.

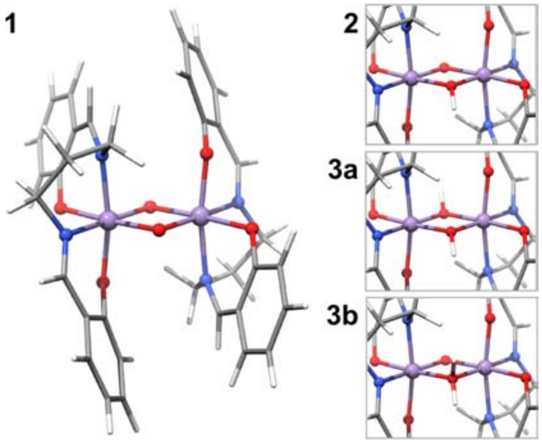

Figure 2. Fully optimized structure of **1** and details of the protonated cores of **2**, **3a** and **3b**. Color code for the atoms as follows: Mn purple, O red, N blue, C gray, H white.

Chart 1. Representation of the Dinuclear $[LMn^{IV}O]_2H_x$ (x = 0−2) Compounds, Their Total Charges and the Selected Core Bond Distances from DFT Geometry Optimization[28a]

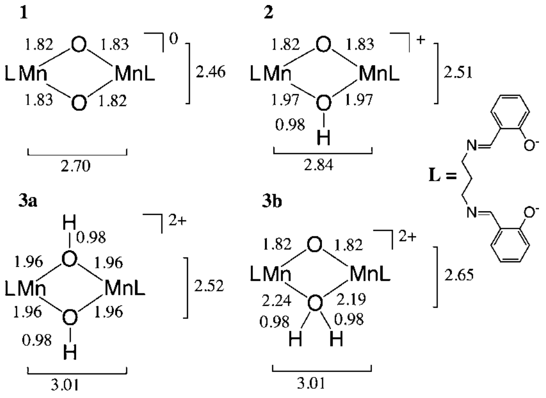

[a] L stands for the salpn ligand.[29] Comparison with EXAFS data[29] and bond angles are given in Chart S1 in the Supporting Information.

complex (Chart 1). Although a symmetric doubly protonated bridging motif is chemically more reasonable, we wish to explore the ability of valence-to-core XES and the accompanying DFT calculations to distinguish between these isomers. Such aquo units have been formulated recently as bridging motifs for the Mn_4CaO_5 core of the oxygen evolving complex (OEC).[37]

■ MATERIALS AND METHODS

XES Measurements. XES measurements were performed on beamline 6-2 at SSRL, with an operating ring current of 300 mA. The beamline monochromator, using two cryogenically cooled Si crystals in (111) reflection, was used to set the incident photon energy to 10.4 keV. The X-ray beam was focused to 0.6 (V) × 0.5 (H) mm (fwhm) by means of vertical and horizontal focusing mirrors. The X-ray flux at 10.4 keV was 3.0×10^{12} photons $\times$ s^{-1} $\times$ mm^{-2}. Multiple spots were used for collecting each XES spectrum, and the total amount of photons deposited on each sample spot was 2.7×10^{12} photons, which is below the threshold of radiation damage determined by XAS (ref 28). Samples were kept at a temperature of 10 K in a liquid helium flow cryostat.

Emission spectra were recorded by means of a high-resolution crystal-array spectrometer, using the 440 reflection of 14 spherically bent Si(110) crystals (100 mm diameter, 1 m radius of curvature), aligned on intersecting Rowland circles.[30] An energy-resolving Si drift detector (Vortex) was positioned at the focus of the 14 diffracting elements. A helium-filled polyethylene bag was placed between the cryostat and the spectrometer to minimize signal attenuation due to air absorption.

The fluorescence signal from the sample was divided by the incident flux (I_0), as monitored by a helium-filled ionization chamber. Spectra were calibrated using MnO as a reference. The first moments of the $K\beta_{1,3}$ and $K\beta_{2,5}$ peaks of a MnO spectrum were calibrated to 6491.00 and 6534.25 eV, respectively.[36] Data were collected at 10 K in a continuous flow liquid helium cryostat (Oxford Instruments CF1208) under helium exchange gas atmosphere.

Analysis of XES Spectra. The XES spectra were fit using the program BlueprintXAS.[38] For each compound, ~100 fits of the $K\beta$ main line and valence to core regions were generated, and at least 90 reasonable fits were included for a statistically significant average (results are reported in Table 1, see Figure S2 in the Supporting Information for second derivatives). All of the emission spectra are normalized to a total integrated area of 1000. Reported experimental areas are based on the average of all good fits. Due to errors in normalization, background subtraction and fitting, a 10% error in the reported areas is estimated.[35] To appropriately and quantitatively compare the calculated XES spectra with the experimental data, the valence-to-core regions were analyzed in a comparable fashion, yielding intensity-weighted average energies (IWAE) and areas of fit or calculated peaks. The direct comparability of these parameters was established in ref 39. The reported experimental peak areas and IWAEs are those of the best-fit averages.

Table 1. Experimental and Calculated Intensity Weighted Average Energies (eV) and Areas for Total Valence-to-Core Regions[a]

	experiment		calculation	
calculation	area	IWAE (eV)	area	IWAE (eV)
1	45.40	6529.2	19.13	6530.8
2	41.28	6528.5	19.76	6530.6
3a	43.94	6528.7	18.70	6531.0
3b			18.28	6530.7

[a] Calculated areas correspond to the sums of the oscillator strengths of the predicted transitions and are multiplied with 1000, but otherwise unscaled. Calculated IWAEs are shifted by 59.2 eV.

Computation of XES Spectra. Valence-to-core X-ray emission spectra were calculated with the one-electron DFT approach implemented in the ORCA program package.[40] The geometries for these calculations were obtained from full relaxations of the crystal structure for compound **1**, with the correct number of protons added in the appropriate positions. These calculations used the BP86 functional[41,42] with the scalar-relativistically recontracted[43] Karlsruhe triple-ζ def2-TZVP(-f) basis set.[44] More details on the geometry optimization are given in ref 28. The method for calculating XES spectra has been published and tested.[35,36] The present paper follows the latter publication in correcting the molecular orbitals for spin−orbit coupling, with the spin−orbit mean-field approximation (SOMF) for the SOC operator.[44,45] The functional BP86 with def2-TZVP(-f) and def2-TZV/J basis sets and the conductor like screening model (COSMO[46]) for dichloromethane (ε = 9.08) was used here. The resulting computed spectra were energy-shifted by 59.2 eV to higher energy and broadened by 3.5 eV as discussed in ref 36. Additionally, the intensity of the calculated spectra was divided by two, since contributions from two donor sites are considered in the calculations, but the experimental normalization procedures result in spectra normalized to only one donor site. To understand the character of the calculated spectral features, it is sufficient to analyze the donor orbital character, since a one-electron picture was employed.

■ RESULTS AND DISCUSSION

When the $[Mn^{IV}(salpn)(O)]_2$ dimer was originally reported, X-ray crystal structures of the protonated species were not available.[29] The protonation states of the oxo bridges were inferred from IR and UV−visible spectroscopy as well as XAS techniques. Using the changes in Mn−ligand and Mn−Mn distances, it was deduced that the protonation of the oxo bridges proceeded from a bis-μ-oxo through a μ-oxo-μ-hydroxo and finally to a bis-μ-hydroxo complex. To test the sensitivity of valence-to-core XES to different types of oxo-bridge protonation patterns, not only a bis-μ-hydroxo complex was considered in the calculations but also a μ-oxo-μ-aquo species. With the complementary approaches of XES and XAS data (in the preceding paper[28]), combined with spectral calculations, it is possible to identify the protonation states of the bridges definitively as described below.

XES Spectra. The $K\beta$ emission spectra consist of the $K\beta'$ and $K\beta_{1,3}$ features, that together are called the main line, and the significantly less intense valence-to-core region at higher energy. The main line extends from 6472 to 6500 eV and is shown in Figure 3. There is a small shift of the $K\beta_{1,3}$ highest energy fit component maximum to higher energy upon

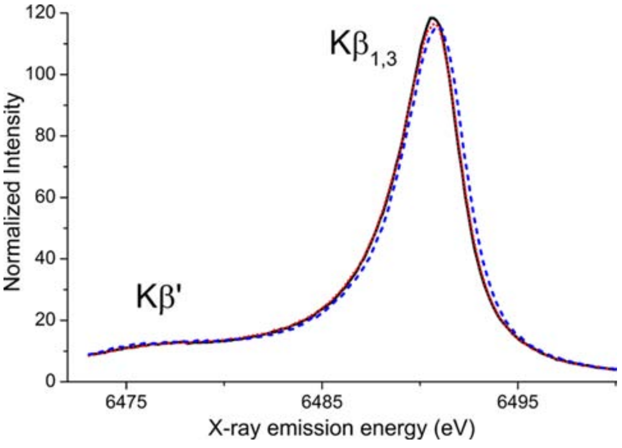

Figure 3. Main line of the X-ray emission spectra of compounds **1** (solid black), **2** (dotted red) and **3** (dashed blue).

protonation of the bridging oxygen atoms, however the magnitude is less than 0.25 eV and thus not sufficiently significant to correspond to changes in the Mn oxidation states. These small changes are consistent with the lack of XAS edge energy changes.[28] It was shown previously that the dominant factor increasing the $K\beta_{1,3}$ energy for Mn monomers is an increased 3p−3d exchange interaction.[36] Since the 3p−3d exchange interaction can be linked to covalency, it is worthwhile to consider the changes in covalency across the series. At each protonation step, the covalency of the Mn−O bonds in the core decreases: the bis-μ-O core is the most covalent and the bis-μ-OH core the least covalent. The decrease in covalency of the bridging motifs should increase the 3p−3d exchange interaction across the series, which may explain the slightly larger splitting of the $K\beta'$ and $K\beta_{1,3}$ features upon protonation and hence the small shifts observed in the $K\beta_{1,3}$ features.

The valence-to-core XES region shows two characteristic peaks, the $K\beta''$ at 6511−6522 eV and the $K\beta_{2,5}$ at 6522−6540 eV (Figure 4a). Clear changes were observed for the three compounds with different protonation states (**1**−**3** in Chart 1): both $K\beta_{2,5}$ and $K\beta''$ features shift to lower energy upon protonation, accompanied by a decrease in peak intensity. For compounds **2** and **3**, a shoulder at the lower-energy side of the $K\beta_{2,5}$ peak grows in (~6530 eV). To emphasize the differences between the spectra for the three models, Figure S1 in the Supporting Information shows the difference spectra of **2** with **1** and **3** with **1**.

The fits to the XES data are composed of a background, which is the sum of the contributions from the $K\beta$ main line features ($K\beta'$ and $K\beta_{1,3}$), and four to six features in the valence-to-core region (see Figure 4b−d). The total areas and IWAEs from the fits are given in Table 1.

$K\beta''$ Region. The $K\beta''$ peaks are due to transitions from molecular orbitals of primarily ligand *n*s character. As ligand *n*s orbitals minimally participate in bonding with the metal, these features serve as excellent probes of ligand identity.[30−36] Focusing on the spectral shape in the 6511−6522 eV spectral range of Figure 4a, one can visually observe an intense and relatively narrow signal for compound **1** at 6519 eV (solid black), a less intense and broad signal for compound **2** between 6516 and 6519 eV (dotted red), and again a relatively narrow signal with the lowest intensity of the series for compound **3** at 6516 eV (dashed blue). The fits in this spectral region distinguish two peaks for compounds **1** and **2**, while for compound **3**, only a single peak component is observed (see Figure 4). For the bis-μ-O bridged complex **1**, the feature at higher energy has a smaller area than the one at lower energy. In compound **2**, there are two features at similar energies to those for compound **1**, but here the higher energy component is less intense while the lower energy component is of comparable intensity. In contrast, a single feature is observed for complex **3**, which has a lower intensity than the combined intensities of the two components in **1** and is shifted toward lower energies compared to the peaks with larger areas of compounds **1** and **2**.

For the three compounds, the ligands are either oxygen-based (bridging oxo and hydroxo, salpn O) or nitrogen-based (salpn N). The protonation of the oxo bridges has a larger influence on the equatorial Mn−O/N_{salpn} bond lengths than on the axial metal−ligand distances: here, the change is 0.11 Å for O_{salpn} and 0.10 Å for N_{salpn} between **1** and **3a**. The axial bond lengths change much less (0.06 Å for O_{salpn}, 0.01 Å for N_{salpn}

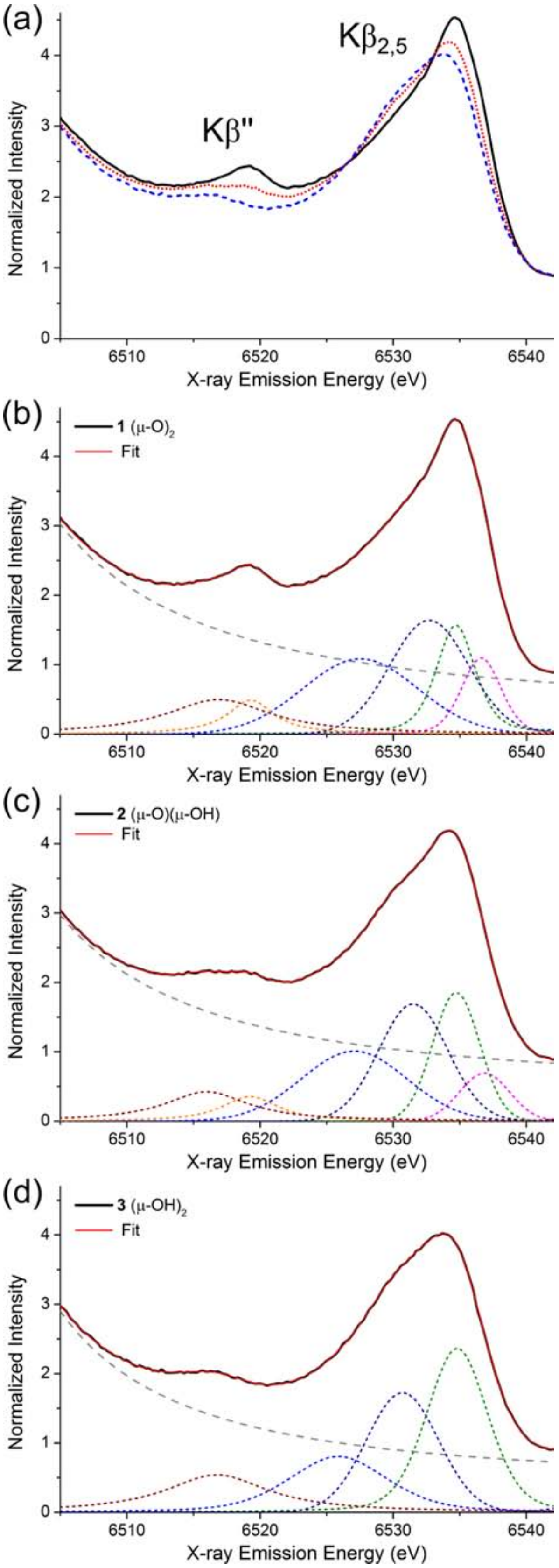

Figure 4. (a) Valence-to-core region of the X-ray emission spectra of compounds **1** (solid black), **2** (dotted red), and **3** (dashed blue). (b−d) Fits to the spectra of compounds **1**−**3**. Second derivatives of the background-subtracted normalized data are given as Figure S2 in the Supporting Information.

between **1** and **3a**). Since the equatorial distance changes are relatively large, one cannot necessarily expect the ligand contributions to be constant, but for extensive ligand systems, the contributions in the valence-to-core region are expected to be relatively small.[35,36] It can thus be expected that the fit component at higher energies is due to transitions from O_{bridge} 2s orbitals, whereas the one at lower energies is due to transitions from OH_{bridge} 2s and N/O_{salpn} 2s orbitals. We assign the spectra with the help of DFT calculations (*vide infra*).

$K\beta_{2,5}$ Region. Here, in the 6522−6540 eV energy range, the main change upon protonation is a systematic decrease in intensity of the main feature at ~6535 eV and a concomitantly increasing shoulder at its lower energy side, ~6530 eV. In the fits, the $K\beta_{2,5}$ region consists of three to four components (see Figure 4b−d). The intensity increase of the low energy shoulder with each protonation event is due to the decrease in the one or two components at highest energy and a shift of the components displayed in light and dark blue to lower energy. Thus, the whole $K\beta_{2,5}$ region becomes broader with successive protonation of the bridging oxo groups.

Upon protonation of the bridging oxygen atoms, the IWAE of the total valence-to-core region increases slightly, from 6529.2 eV (**1**: bis-*μ*-O) to 6528.5 eV (**2**: (*μ*-O)(*μ*-OH)) and to 6528.7 eV (**3**: bis-*μ*-OH). The peak areas change more significantly, from 45.40 (**1**: bis-*μ*-O) to 41.28 (**2**: (*μ*-O)(*μ*-OH)) and to 43.94 (**3**: bis-*μ*-OH).

Calculated XES. The calculated valence-to-core XES spectra for models **1**, **2**, **3a** and **3b** are shown in Figure 5, and the IWAEs and peak positions are summarized in Table 1. The general trends in both the $K\beta''$ (6511−6525 eV) and the $K\beta_{2,5}$ (6525−6540 eV) regions are well-reproduced. The $K\beta''$ feature in the calculated spectrum of compound **1** is located at the highest energy compared to the other features in the series (6520.4 eV, black in Figure 5) and is predicted to have an asymmetric narrow peak in agreement with experiment. The calculated spectrum of the doubly protonated species **3a** shows a similarly narrow but symmetric feature appearing at the lowest energy of this series (~6518.5 eV, blue in Figure 5), reproducing the experimental trend. Most importantly, the width of the $K\beta''$ peak of compound **2** is the broadest in this region, which is in excellent agreement with the experimental data. In fact, the broad calculated $K\beta''$ peak of compound **2** extends from the lower energy end of compound **3a** to nearly the higher energy end of compound **1**. This is also predicted to be the case for the spectrum of the putative complex **3b**. To higher energies, in the $K\beta_{2,5}$ region between 6524 and 6540 eV, the intensity of the main feature at ~6535 eV decreases upon protonation. Just as in the experimental spectra, the shoulder at ~6530 eV increases in intensity between the unprotonated and the protonated complexes.

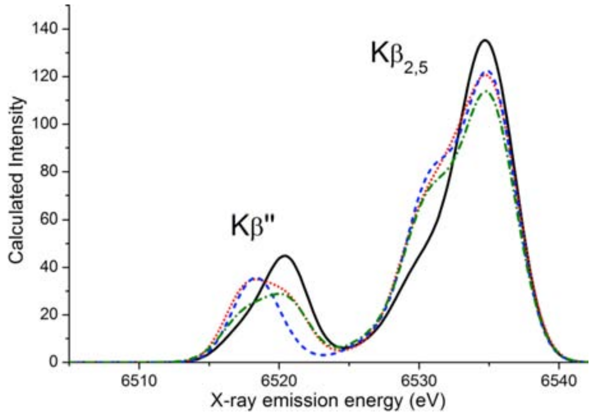

Figure 5. Calculated valence-to-core spectra of compounds **1** (solid black), **2** (dotted red), **3a** (dashed blue), and **3b** (dashed-dotted green). Calculated spectrum is shifted by 59.2 eV.

Regarding the ability of XES to distinguish the symmetric (**3a**, dihydroxo) vs the asymmetric (**3b**, oxo-aqua) doubly protonated species, we note that the spectra of complexes **3a** and **3b** differ in the intensity distribution of the $K\beta''$ region. The spectrum of **3a** reproduces a narrow, intense feature shifted to lower energies compared to that of **1**, whereas the spectrum of **3b** is broad and of low intensity. Thus, the spectrum of **3a** yields a better match with experiment than that of **3b**. This is also in line with the calculated energetic and magnetic data for both structural proposals.[28]

The fact that the $K\beta''$ regions of **2** and **3** are clearly distinguished by experiment and the demonstration that models **2**, **3a**, and **3b** are computationally distinct give confidence in the ability of valence-to-core XES to differentiate not only between complexes in different protonation states (bis-*μ*-oxo, *μ*-oxo-*μ*-hydroxo, bis-*μ*-hydroxo) but also between complexes of the same nuclearity with different bridging motifs (bis-*μ*-hydroxo, *μ*-oxo-*μ*-aquo).

Assignments of the $K\beta''$ Region. Figure 6 shows the origin of the $K\beta''$ and $K\beta_{2,5}$ regions of the valence-to-core spectra, determined on the basis of the calculated spectra. The $K\beta''$ feature arises from electronic transitions from O and N 2s into Mn 1s orbitals. The O_{salpn} 2s and N_{salpn} 2s contributions appear at the same energies in all spectra, and thus can serve as reference points. For compound **1**, the transitions appear in the order O_{salpn} 2s, N_{salpn} 2s, O_{bridge} 2s from lower to higher energy, where the O_{bridge} 2s components are the most intense. The O_{bridge} 2s and O_{salpn} 2s transitions are separated by ~3 eV according to the calculations. Upon single protonation, yielding **2**, no energetic shifts are observed for transitions from the O_{bridge} 2s orbitals with respect to their positions in the spectrum of **1**, whereas the transitions from the single-protonated bridging oxygen atoms (OH_{bridge} 2s) are shifted into the energy region of the O_{salpn} 2s transitions. Inspection of the isosurfaces representing the donor orbitals of these transitions reveals that the orbitals have mixed O_{salpn} 2s/O_{bridge} 2s character (see Figure 7). The broad feature of the $K\beta''$ peak in compound **2** can thus be explained by the distinct energy separation of ~3 eV between the protonated and unprotonated oxo-bridge 2s orbitals. In the doubly protonated compound **3a**, the OH_{bridge} 2s components appear at energies between the O_{salpn} 2s and N_{salpn} 2s ones, their close energy levels making the $K\beta''$ feature appear as a single peak. For compound **3b**, the H_2O_{bridge} 2s components are found at energies lower than those of O_{salpn} 2s, which increases the asymmetry of the $K\beta''$ feature and broadens it relative to the peak of compound **3a**. The O_{bridge} 2s position is the same as those observed in the compounds **1** and **2**.

In short, the $K\beta''$ region of Mn^{IV} dimers with protonated or unprotonated oxo bridges can be attributed to transitions from O_{bridge} 2s, O_{salpn} 2s and N_{salpn} 2s orbitals. The energetic positions of the O_{bridge} 2s transitions shift by more than 3 eV upon protonation, significantly broadening the spectra. Regarding the relative intensities, the approximate order is calculated to be O_{bridge} 2s $\gg$ OH_{bridge} 2s > O_{salpn} 2s > N_{salpn} 2s $\gg$ H_2O_{bridge} 2s. The reason for the strong contribution of transitions from O_{bridge} 2s orbitals to the envelope intensity is

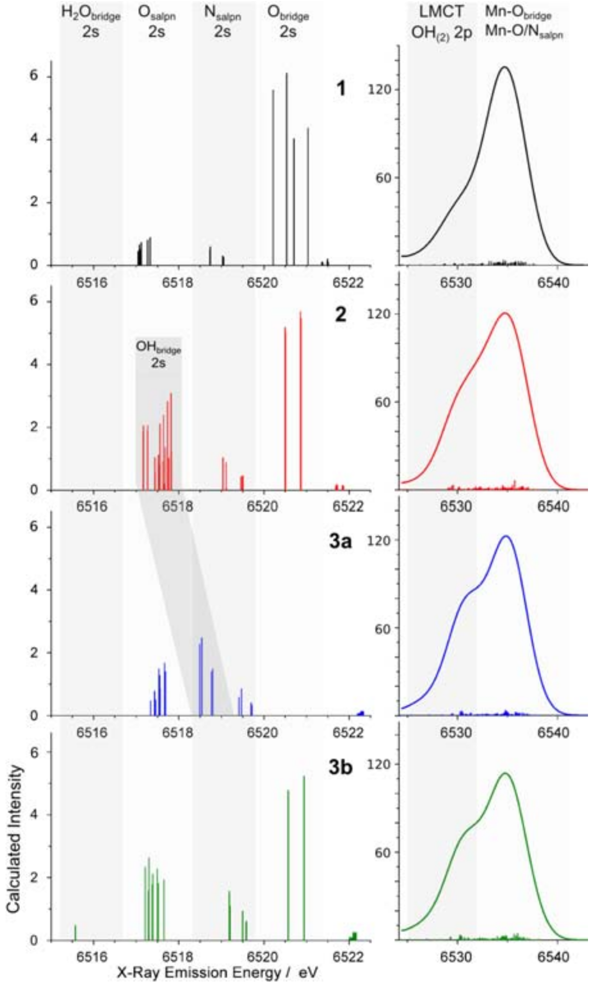

Figure 6. Assignments of the calculated XES valence-to-core region based on the orbital character corresponding to the individual transitions for compounds **1** (a), **2** (b), **3a** (c) and **3b** (d). The left side shows the Kβ'' region, and the right side shows the K$\beta_{2,5}$ region with different intensity scales. Gray areas where transitions of different donor orbital character appear; from left to right: H$_2$O$_{bridge}$ 2s, O$_{salpn}$ 2s, N$_{salpn}$ 2s, O$_{bridge}$ 2s in the left half; OH/OH$_2$ 2p and LMCT, Mn−O/N$_{salpn}$ and Mn−O$_{bridge}$ in the right half. Transitions from orbitals with OH$_{bridge}$ 2s character are found either in the O$_{salpn}$ 2s region (mixed with O$_{salpn}$ 2s character) or separately in the N$_{salpn}$ 2s energy region (darkest gray). Representative donor orbitals for each of the spectral regions are shown in Figure 7.

attributed to the shorter Mn−O$_{bridge}$ than Mn−O$_{salpn}$ distances. Mn−O$_{bridge}$ distances of 1.81−1.82 Å were obtained from the crystal structure in compound **1**, whereas Mn−O$_{salpn}$ and Mn−N$_{salpn}$ distances in this complex are much longer (1.91−1.93 Å and 2.00−2.06 Å, respectively). This trend is reproduced in the DFT calculations, where Mn−O$_{bridge}$ distances of 1.82−1.83 Å and longer Mn−O$_{salpn}$ and Mn−N$_{salpn}$ distances (1.93−1.95 Å, 2.00−2.05 Å) were obtained for **1**.[28] Upon protonation of the bridging oxygen atoms, the Mn−OH$_{bridge}$ distance is expected to increase to ~1.97 Å based on the DFT optimized geometry. The elongation of the bridging oxygen atoms upon protonation is consistent with the EXAFS results (for details, see the Supporting Information and the preceding XAS paper[28]). The Kβ'' components of these protonated oxo bridges have lower intensities due to the lower overlap of the donor with the acceptor orbitals, which is linked to the distance between donor site and acceptor site. Based on the distance argument only, one would then expect lower intensities for transitions originating from OH$_{bridge}$ 2s orbitals than for those from O$_{salpn}$ 2s orbitals (Mn−O distances of 1.97 Å and 1.84−1.87 Å in **3a**, respectively). The slightly higher intensities found in the calculations (Figure 6, **3a** panel) can be explained with the more localized O 2s character in ligands of smaller size,[48] leading to more intense transitions from the OH bridge than from the O atoms in the salpn ligand. For a bridging aquo ligand, the Mn−H$_2$O$_{bridge}$ distance will be further elongated (~2.2 Å) and the donor orbital less localized, and indeed these transitions are computed to be the least intense (Figure 6, **3b** panel).

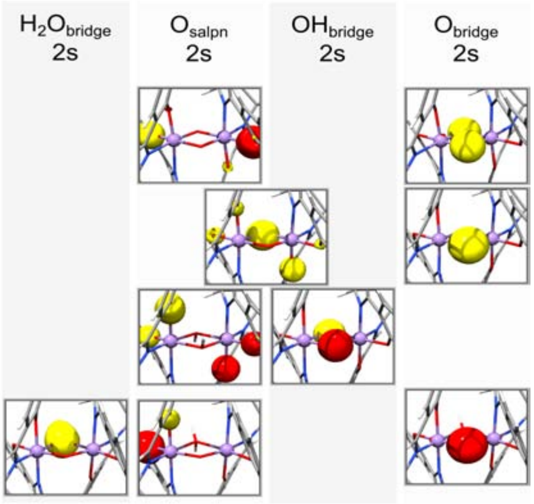

Figure 7. Representative donor orbitals corresponding to each of the assigned regions of the Kβ'' peak in Figure 6 (except "N$_{salpn}$ 2s", instead "OH$_{bridge}$ 2s" is shown in a separate panel); from top to bottom: bis-μ-oxo (**1**), μ-oxo-μ-hydroxo (**2**), bis-μ-hydroxo (**3a**), μ-oxo-μ-aquo (**3b**).

Assignments of the K$\beta_{2,5}$ Region. The calculated K$\beta_{2,5}$ main features of the three compounds exhibit no major energy shifts, whereas the decrease in peak intensity upon protonation is significant. In agreement with experiment, the area of the total K$\beta_{2,5}$ region shows little variation. In compound **1**, the shoulder at ~6530 eV originates from transitions of LMCT (ligand−metal charge transfer) character from the salpn ligand. The increase in the shoulder intensity in compounds **2** and **3** stems from additional transitions out of hydroxo-bridge orbitals of p-character, that fall into the same energy region. The most intense peak is largely due to transitions from Mn−O/N$_{salpn}$ 2p and Mn−O$_{bridge}$ 2p based molecular orbitals (see Figure 6).

Correlation of Experimental and Calculated Valence-to-Core Regions. Although, from visual inspection only, the agreement of calculation and experiment is good, it is worthwhile to quantify the agreement by correlating the experimental and calculated areas. The X-ray emission spectra are compared to a previously published set of monomer data that includes Mn(II) as well as Mn(III) and Mn(IV) data.[36] Figure 8 shows the correlation, where the trendline based on all data points is forced through 0 and follows $y = 0.477x$. The adjusted R value of 0.992 indicates good agreement between experiment and calculation. More details on the monomer data and the error bars are given in the Supporting Information.

Based solely on this correlation, it is not possible to discriminate between the bridging motifs of **3a** and **3b**. However, the differences in the Kβ'' intensity distributions in

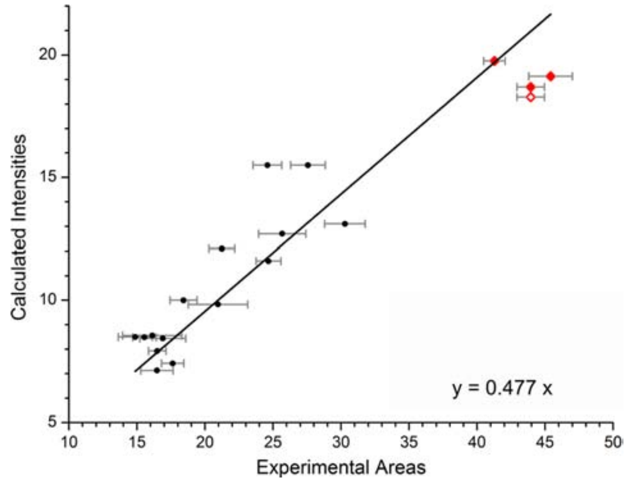

Figure 8. Correlation of experimental and calculated areas. Red diamonds correspond to the areas of the dimers; the unfilled red diamond corresponds to data for dimer **3b**. Monomer data are shown as black circles. The linear regression line is based on both the monomer and the dimer data and forced through 0. It follows the equation $y = 0.477x$ with an adjusted R value of 0.992.

the 6511−6522 eV spectral region clearly show that, for the symmetric compounds **1** and **3**, narrow signals at different energies are observed whereas, for the asymmetric compound **2**, a broad Kβ'' feature is observed. Thus, the envelopes help to understand the differences between the calculated spectra of **3a** and **3b** compared to the experimental one. For lower-resolution data, it is however crucial to make use of the complementarity of X-ray absorption and emission spectroscopy. As is presented in ref 28, the pre-edge areas for compound **3b** are clearly outside the correlation range.

■ CONCLUSION

In this study, we have demonstrated that XES valence to core spectra probe the ligand environment of metals with great sensitivity, including single protonation events. In particular, the Kβ'' satellite peaks can be used to discriminate among a set of three Mn^{IV} dimers in which the protonation states of bridging oxygen atoms are changed systematically. The limits of structure discrimination were further explored by comparison to calculated spectra for the two isomers $[\mathrm{Mn^{IV}_2(salpn)_2(\mu\text{-}OH)_2}]^{2+}$ and $[\mathrm{Mn^{IV}_2(salpn)_2(\mu\text{-}OH)(\mu\text{-}OH_2)}]^{2+}$. We find that even such fine differences can be reliably evaluated by DFT calculations, and given the size of these spectral changes they should also be experimentally observable. The application of these methods to metalloprotein active sites will certainly pose greater challenges. However, the observation of single light atoms from valence-to-core XES has already been demonstrated for both nitrogenase and the OEC.[32,33] The determination of more subtle changes, such as single protonation events within the OEC active site, may be addressed by utilizing difference spectra to highlight the changes between different S states. The $\mathrm{Mn_4CaO_5}$ complex has a ligation sphere that may be composed of oxygen-derived ligands (including O^{2-}, OH^-, and/or H_2O), carboxylate ligands and histidine ligands. While all of these ligands will contribute to the K$\beta_{2,5}$ region of the spectrum, the most significant intensity in the Kβ'' region will derive from OH^- or O^{2-} ligands. As the present study shows, the changes between oxo and hydroxo groups should result in clear spectral changes, which may be highlighted by examining spectral differences. The observation of such (de)protonation events at manganese-bound oxo bridges should provide fundamental insights toward understanding of the catalytic cycle of the OEC, as well as other enzymes featuring dinuclear, high-valent manganese ions in their active sites, such as manganese RnR or manganese catalase.[2,47]

The assignments of the valence-to-core region show that the transitions of largest intensity in the Kβ'' region are due to transitions from the oxo-bridge 2s orbitals, which are significantly more intense than transitions from salpn-N/O 2s or hydroxo/aquo-bridge 2s orbitals. This is attributed to the shorter Mn−O distance and more localized donor orbital character in the unprotonated bridges, leading to larger overlap of donor and acceptor orbitals and hence more intense transitions. In the K$\beta_{2,5}$ region, a shoulder in the lower energy range is shown to be indicative of bridging hydroxo 2p contributions which are only present in protonated species, leading to increased intensity in this region across the series.

The data presented here demonstrate the exquisite chemical sensitivity of valence-to-core XES, which is further strengthened when combined with X-ray absorption spectroscopy.[28] Together these two techniques provide powerful element-specific tools to monitor changes in the ligand environment in metalloproteins, possibly during catalysis, by neglecting the overwhelming number of surrounding light atoms. A further challenge will be to detect protonation state changes that occur at terminal ligands in multinuclear complexes, and such studies are underway.

■ ASSOCIATED CONTENT

Ⓢ Supporting Information

Full geometry details (Chart S1). Experimental valence-to-core difference spectra (Figure S1). 2nd derivatives of the valence-to-core background-subtracted spectra (Figure S2). Examples of input files for XES calculations. Reference monomer data including standard deviations (Table S1). This material is available free of charge via the Internet at http://pubs.acs.org.

■ AUTHOR INFORMATION

Corresponding Authors

*E-mail: serena.debeer@cec.mpg.de.
*E-mail: vlpec@umich.edu.
*E-mail: jyano@lbl.gov.

Present Addresses

B.L.-K.: Synchrotron SOLEIL, L'Orme des Merisier, BP 48 Saint-Aubin, 91192 Gif sur Yvette, France.

T.T.B.: Department of Chemistry, Slippery Rock University, 272 Advanced Technology and Science Hall #264, Slippery Rock, PA 16057, United States.

H.S.: Helmholtz-Zentrum Berlin für Materialien and Energie GmbH, Albert-Einstein-Strasse 15, 12489 Berlin, Germany. Institut für Physik and Astronomie, Universität Potsdam, Karl-Liebknecht-Strasse 24/25, 14476 Potsdam, Germany.

Author Contributions

B.L.-K., T.T.B., and V.K. contributed equally to the manuscript.

Notes

The authors declare no competing financial interest.

■ ACKNOWLEDGMENTS

This work was supported by the Director, Office of Science, Office of Basic Energy Sciences (OBES), Division of Chemical

Sciences, Geosciences, and Biosciences (CSGB) of the Department of Energy (DOE) under Contract DE-AC02-05CH11231 (J.Y. and V.K.Y.) for instrumentation development and NIH Grant GM 55302 (V.K.Y) for Mn inorganic chemistry. Experiments were carried out at Stanford Synchrotron Radiation Lightsource (SSRL), BL 6-2 in Stanford. SSRL is supported by DOE OBER. We thank the staff at SSRL for their support. V.K., M.A.B., S.D. and F.N. thank the Max Planck Society for funding. Also S.D. acknowledges Cornell University and the Alfred P. Sloan Foundation for fellowship. Christopher J. Pollock and Eleanor R. Hall are acknowledged for assistance with fits to the experimental spectra.

■ REFERENCES

(1) Whittaker, M. M.; Barynin, V. V.; Igarashi, T.; Whittaker, J. W. *Eur. J. Biochem.* **2003**, *270*, 1102−1116.

(2) Barynin, V. V.; Whittaker, M. M.; Antonyuk, S. V.; Lamzin, V. S.; Harrison, P. M.; Artymiuk, P. J.; Whittaker, J. W. *Structure* **2001**, *9*, 725−738.

(3) Sproviero, E. M.; Gascon, J. A.; McEvoy, J. P.; Brudvig, G. W.; Batista, V. S. *Coord. Chem. Rev.* **2008**, *252*, 395−415.

(4) Siegbahn, P. E. M. *Acc. Chem. Res.* **2009**, *42*, 1871−1880.

(5) Yamanaka, S.; Kanda, K.; Saito, T.; Umena, Y.; Kawakami, K.; Shen, J.-R.; Kamiya, N.; Okumura, M.; Nakamura, H.; Yamaguchi, K. In *Advances in Quantum Chemistry*; Elsevier: 2012; Vol. *64*, pp 121−187.

(6) Mahapatra, S.; Halfen, J. A.; Wilkinson, E. C.; Pan, G. F.; Wang, X. D.; Young, V. G.; Cramer, C. J.; Que, L.; Tolman, W. B. *J. Am. Chem. Soc.* **1996**, *118*, 11555−11574.

(7) Berreau, L. M.; Mahapatra, S.; Halfen, J. A.; Houser, R. P.; Young, V. G.; Tolman, W. B. *Angew. Chem., Int. Ed.* **1999**, *38*, 207−210.

(8) Mahapatra, S.; Halfen, J. A.; Wilkinson, E. C.; Que, L.; Tolman, W. B. *J. Am. Chem. Soc.* **1994**, *116*, 9785−9786.

(9) Bollinger, J. M.; Jiang, W.; Green, M. T.; Krebs, C. *Curr. Opin. Struct. Biol.* **2008**, *18*, 650−657.

(10) Lee, S. K.; Nesheim, J. C.; Lipscomb, J. D. *J. Biol. Chem.* **1993**, *268*, 21569−21577.

(11) Lee, S. K.; Fox, B. G.; Froland, W. A.; Lipscomb, J. D.; Munck, E. *J. Am. Chem. Soc.* **1993**, *115*, 6450−6451.

(12) Hsu, H. F.; Dong, Y. H.; Shu, L. J.; Young, V. G.; Que, L. *J. Am. Chem. Soc.* **1999**, *121*, 5230−5237.

(13) Stubna, A.; Jo, D. H.; Costas, M.; Brenessel, W. W.; Andres, H.; Bominaar, E. L.; Munck, E.; Que, L. *Inorg. Chem.* **2004**, *43*, 3067−3079.

(14) Kryatov, S. V.; Taktak, S.; Korendovych, I. V.; Rybak-Akimova, E. V.; Kaizer, J.; Torelli, S.; Shan, X. P.; Mandal, S.; MacMurdo, V. L.; Payeras, A. M. I.; Que, L. *Inorg. Chem.* **2005**, *44*, 85−99.

(15) Mukhopadhyay, S.; Mandal, S. K.; Bhaduri, S.; Armstrong, W. H. *Chem. Rev.* **2004**, *104*, 3981−4026.

(16) Parsell, T. H.; Behan, R. K.; Green, M. T.; Hendrich, M. P.; Borovik, A. S. *J. Am. Chem. Soc.* **2006**, *128*, 8728−8729.

(17) Yin, G.; Danby, A. M.; Kitko, D.; Carter, J. D.; Scheper, W. M.; Busch, D. H. *J. Am. Chem. Soc.* **2008**, *130*, 16245−16253.

(18) Lassalle-Kaiser, B.; Hureau, C.; Pantazis, D. A.; Pushkar, Y.; Guillot, R.; Yachandra, V. K.; Yano, J.; Neese, F.; Anxolabehere-Mallart, E. *Energy Environ. Sci.* **2010**, *3*, 924−938.

(19) Martinho, M.; Banse, F.; Bartoli, J.-F.; Mattioli, T. A.; Battioni, P.; Horner, O.; Bourcier, S.; Girerd, J.-J. *Inorg. Chem.* **2005**, *44*, 9592−9596.

(20) Bigi, J. P.; Harman, W. H.; Lassalle-Kaiser, B.; Robles, D. M.; Stich, T. A.; Yano, J.; Britt, R. D.; Chang, C. J. *J. Am. Chem. Soc.* **2012**, *134*, 1536−1542.

(21) Yin, G. C.; Danby, A. M.; Kitko, D.; Carter, J. D.; Scheper, W. M.; Busch, D. H. *J. Am. Chem. Soc.* **2007**, *129*, 1512−1513.

(22) Fiedler, A. T.; Que, L. *Inorg. Chem.* **2009**, *48*, 11038−11047.

(23) Jensen, M. P.; Costas, M.; Ho, R. Y. N.; Kaizer, J.; Payeras, A. M. I.; Munck, E.; Que, L.; Rohde, J. U.; Stubna, A. *J. Am. Chem. Soc.* **2005**, *127*, 10512−10525.

(24) MacMurdo, V. L.; Zheng, H.; Que, L. *Inorg. Chem.* **2000**, *39*, 2254−2255.

(25) Noguchi, T. *Philos. Trans. R. Soc., B* **2008**, *363*, 1189−1194.

(26) Milikisiyants, S.; Chatterjee, R.; Lakshmi, K. V. *J. Phys. Chem. B* **2011**, *115*, 12220−12229.

(27) Su, J. H.; Cox, N.; Ames, W.; Pantazis, D. A.; Rapatskiy, L.; Lohmiller, T.; Kulik, L. V.; Dorlet, P.; Rutherford, A. W.; Neese, F.; Boussac, A.; Lubitz, W.; Messinger, J. *Biochim. Biophys. Acta, Bioenerg.* **2011**, *1807*, 829−840.

(28) Krewald, V.; Lassalle-Kaiser, B.; Boron, T. T., III; Pollock, C. J.; Kern, J.; Beckwith, M. A.; Yachandra, V. K.; Pecoraro, V. L.; Yano, J.; Neese, F.; DeBeer, S. *Inorg. Chem.* **2013**, DOI: 10.1021/ic4008203.

(29) Baldwin, M. J.; Stemmler, T. L.; Riggs-Gelasco, P. J.; Kirk, M. L.; Penner-Hahn, J. E.; Pecoraro, V. L. *J. Am. Chem. Soc.* **1994**, *116*, 11349−11356.

(30) Glatzel, P.; Bergmann, U. *Coord. Chem. Rev.* **2005**, *249*, 65−95.

(31) Bergmann, U.; Bendix, J.; Glatzel, P.; Gray, H. B.; Cramer, S. P. *J. Chem. Phys.* **2002**, *116*, 2011−2015.

(32) Pushkar, Y.; Long, X.; Glatzel, P.; Brudvig, G. W.; Dismukes, G. C.; Collins, T. J.; Yachandra, V. K.; Yano, J.; Bergmann, U. *Angew. Chem., Int. Ed.* **2010**, *49*, 800−803.

(33) Lancaster, K. M.; Roemelt, M.; Ettenhuber, P.; Hu, Y. L.; Ribbe, M. W.; Neese, F.; Bergmann, U.; DeBeer, S. *Science* **2011**, *334*, 974−977.

(34) Smolentsev, G.; Soldatov, A. V.; Messinger, J.; Merz, K.; Weyhermuller, T.; Bergmann, U.; Pushkar, Y.; Yano, J.; Yachandra, V. K.; Glatzel, P. *J. Am. Chem. Soc.* **2009**, *131*, 13161−13167.

(35) Lee, N.; Petrenko, T.; Bergmann, U.; Neese, F.; DeBeer, S. *J. Am. Chem. Soc.* **2010**, *132*, 9715−9727.

(36) Beckwith, M. A.; Roemelt, M.; Collomb, M. N.; DuBoc, C.; Weng, T. C.; Bergmann, U.; Glatzel, P.; Neese, F.; DeBeer, S. *Inorg. Chem.* **2011**, *50*, 8397−8409.

(37) Gatt, P.; Petrie, S.; Stranger, R.; Pace, R. J. *Angew. Chem.* **2012**, *124*, 12191−12194.

(38) Delgado-Jaime, M. U.; Mewis, C. P.; Kennepohl, P. *J. Synchrotron Radiat.* **2010**, *17*, 132−137.

(39) DeBeer George, S.; Petrenko, T.; Neese, F. *J. Phys. Chem. A* **2008**, *112*, 12936−12943.

(40) Neese, F. In *ORCA program*; Version 2.8; Univ. Bonn.

(41) Becke, A. D. *Phys Rev A* **1988**, *38*, 3098−3100.

(42) Perdew, J. P. *Phys. Rev. B* **1986**, *33*, 8822−8824.

(43) Pantazis, D. A.; Chen, X. Y.; Landis, C. R.; Neese, F. *J. Chem. Theory Comput.* **2008**, *4*, 908−919.

(44) Weigend, F.; Ahlrichs, R. *Phys. Chem. Chem. Phys.* **2005**, *7*, 3297−3305.

(45) Hess, B. A.; Marian, C. M.; Wahlgren, U.; Gropen, O. *Chem. Phys. Lett.* **1996**, *251*, 365−371.

(46) Klamt, A.; Schüürmann, G. *J. Chem. Soc., Perkin Trans.* **1993**, *2*, 799−805.

(47) Tomter, A. B.; Zoppellaro, G.; Andersen, N. H.; Hersleth, H.-P.; Hammerstad, M.; Røhr, Å. K.; Sandvik, G. K.; Strand, K. R.; Nilsson, G. E.; Bell, C. B., III; Barra, A.-L.; Blasco, E.; Le Pape, L.; Solomon, E. I.; Andersson, K. K. *Coord. Chem. Rev.* **2013**, *257*, 3−26.

(48) Pollock, C. J.; DeBeer, S. *J. Am. Chem. Soc.* **2011**, *133*, 5594−5601.